and product phases were examined with a 200-kV JEOL-2010 TEM.
8. Electron microprobe analysis of the recovered samples revealed that small, iron-rich grains (less than 10 μm) with olivine stoichiometry exist within the reaction rim especially near the surface. The Mg/(Mg + Fe) ratios in these iron-rich grains range from about 81 to 85. This suggests that the iron-rich grains are ringwoodite, and the transformation occurred in the coexisting field of wadsleyite and ringwoodite at lower temperature before the desired value was reached.
9. F. Guyot, G. D. Gwamnesia, R. C. Liebermann, *Geophys. Res. Lett.* **18**, 89 (1991); A. J. Brearley, D. C. Rubie, E. Ito, *Phys. Chem. Miner.* **18**, 343 (1992); K. Fujino and T. Irifune, in *High Pressure Research: Application to Earth and Planetary Sciences*, Y. Syono and M. H. Manghnani, Eds. (American Geophysical Union, Washington, DC, 1992), pp. 237–244; A. J. Brearley and D. C. Rubie, *Phys. Earth Planet. Int.* **86**, 45 (1994).
10. FTIR measurements were carried out in air. Thickness of the sample was 80 to 140 μm, and aperture size ranged from 50 μm by 50 μm to 500 μm by 500 μm. Water content of wadsleyite was estimated from the integration of the infrared spectra using the calibration by Paterson [M. S. Paterson, *Bull. Mineral.* **105**, 20 (1982)].
11. D. C. Rubie and A. B. Thompson, in *Advances in Physical Geochemistry*, vol. 4., *Metamorphic Reactions: Kinetics, Textures, and Deformation*, A. B. Thompson and D. C. Rubie, Eds. (Springer-Verlag, New York, 1985), pp. 27–79.
12. M. Liu, L. Kerschhofer, and D. C. Rubie [*Eos (Fall suppl.)* **77**, 716 (1996)] considered the effect of the strain energy associated with first-order transformation on the growth rate.
13. S. Morris, *Proc. R. Soc. London Ser. A* **436**, 203 (1992).
14. We thank D. C. Rubie, S. Karato, and J. P. Poirier for suggestions; H. Keppler, T. Terada, and M. Akizuki for the FTIR measurements; and T. Nagase and N. Miyajima for the TEM observation. This work was supported in part by a Grant-in-Aid for Scientific Research (A) (09304051) from the Japanese Ministry of Education, Science, Sports, and Culture (to E.O.).

18 February 1998; accepted 14 May 1998

High-Temperature Silicate Volcanism on Jupiter's Moon Io

A. S. McEwen,* L. Keszthelyi, J. R. Spencer, G. Schubert, D. L. Matson, R. Lopes-Gautier, K. P. Klaasen, T. V. Johnson, J. W. Head, P. Geissler, S. Fagents, A. G. Davies, M. H. Carr, H. H. Breneman, M. J. S. Belton

Infrared wavelength observations of Io by the Galileo spacecraft show that at least 12 different vents are erupting lavas that are probably hotter than the highest temperature basaltic eruptions on Earth today. In at least one case, the eruption near Pillan Patera, two independent instruments on Galileo show that the lava temperature must have exceeded 1700 kelvin and may have reached 2000 kelvin. The most likely explanation is that these lavas are ultramafic (magnesium-rich) silicates, and this idea is supported by the tentative identification of magnesium-rich orthopyroxene in lava flows associated with these high-temperature hot spots.

After the Voyager spacecraft flybys of the Jupiter system in 1979, many investigators thought that the active volcanism on Io was dominated by sulfur-rich lavas, although silicate magmas at depth may have initially melted these lavas (*1*). The highest temperatures estimated from Voyager were ~650 K (*2*), consistent with sulfur volcanism, but Voyager could not detect small areas at higher temperatures because of limitations in sensitivity and wavelength coverage. Ground-based telescopic observations in 1986 provided observations of a temperature exceeding 900 K, suggesting at least occasional eruptions of silicate lavas (*3*). Recent Earth-based and Galileo observations have shown that such high-temperature hot spots are actually common on Io (*4*, *5*). Thirty locations with temperatures higher than 700 K were identified during the Galileo tour in 1996 to 1997; most of these probably include areas with temperatures higher than 1000 K (*6*). These temperatures are well above the boiling point for elemental S in a near vacuum (*7*), so silicate eruptions are now thought to be a fundamental part of Io's active volcanism (*8*).

We report principally on observations of Io in eclipse (in Jupiter's shadow; see Fig. 1) by the Galileo Solid State Imaging (SSI) experiment (*9*). SSI has observed Io during 11 eclipses in the first 11 orbits, including observations through the broadband clear filter and six color filters with effective wavelengths from 0.42 to 0.99 μm. These images revealed (i) small bright spots in the clear and 1MC (~0.99 μm) bandpasses that are due to high-temperature hot spots and (ii) faint diffuse glows due to electronic excitation of gases around the limb and near active vents in the clear and visible bandpasses (*5*, *6*, *10*). The actual area of each hot spot (typically

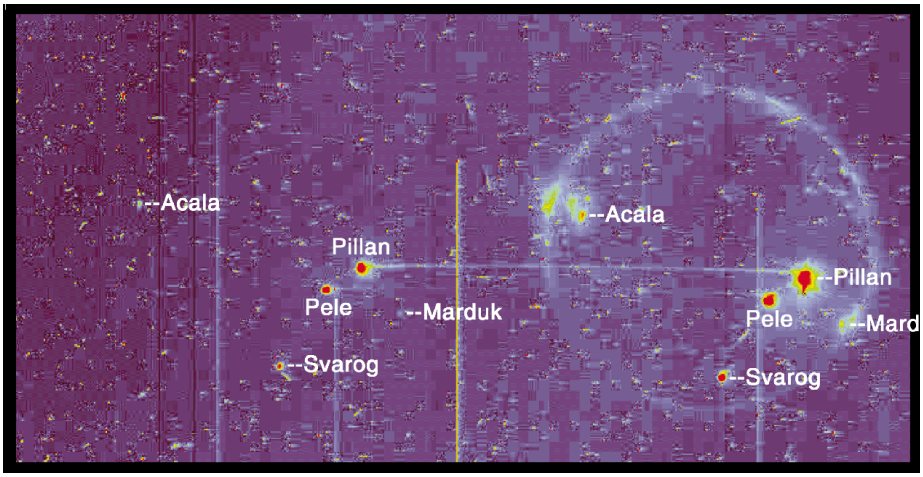

Fig. 1. SSI image showing Io in eclipse (PICNOs C9I0025-26). Image is color coded with blue-yellow-red representing increasing brightness. This image is a "raw" spacecraft frame, with no processing other than color coding and labels, to illustrate several characteristics of the data. The left-hand image was acquired through the 1MC bandpass and the right-hand image is dominated by the clear-filter exposure (plus 1MC exposure). The scale is 14.6 km/pixel, but each hot spot is smeared over an area about nine pixels in diameter. Temperature-area modeling (Table 2) indicates that the actual hot areas are much smaller than the pixels. Diffuse glows from electronic excitation of gases highlight Io's limb and active plumes such as Marduk in the clear-filter image. Small bright pixels and clusters of pixels are noise from radiation hits. The horizontal line between Pillan positions is due to 1MC exposure during scan platform motion. The bright vertical lines are due to column blemishes, and the blockiness at low brightness levels is due to data compression (*9*).

A. S. McEwen, L. Keszthelyi, P. Geissler, Lunar and Planetary Lab, University of Arizona, Tucson, AZ 85711, USA. J. R. Spencer, Lowell Observatory, Flagstaff, AZ 86001, USA. G. Schubert, Department of Earth and Space Sciences, University of California Los Angeles, Los Angeles, CA 90095, USA. D. L. Matson, R. Lopes-Gautier, K. P. Klaasen, T. V. Johnson, A. G. Davies, H. H. Breneman, Jet Propulsion Laboratory, Pasadena, CA 91109, USA. J. W. Head, Department of Geological Science, Brown University, Providence, RI 02912, USA. S. Fagents, Department of Geology, Arizona State University, Tempe, AZ 85287, USA. M. H. Carr, U.S. Geological Survey, Menlo Park, CA 94025, USA. M. J. S. Belton, National Optical Astronomy Observatories, Tucson, AZ 85719, USA.

*To whom correspondence should be addressed. E-mail: mcewen@lpl.arizona.edu

<0.01 km^2) is much smaller than the 11- to 33-km size of each picture element (pixel), but the hot spot signal is smeared over areas ranging from 3 to 29 pixels long because of spacecraft motion during the 0.27- to 25.6-s exposures (Fig. 1).

To estimate temperatures, we used the ratio of the intensities of the clear (0.4 to 1.05 μm) and 1MC (0.968 to 1.05 μm) bandpass images. Such pairs of images were acquired during five eclipses (Table 1). The bandpasses have broad and complex spectral responses, so we cannot determine radiance at any particular wavelength. Instead, we used our knowledge of the calibration of the SSI instrument (*9*) to calculate its response (in electrons per pixel) as a function of blackbody temperature for each bandpass. The ratio of clear and 1MC intensities is a function of temperature (Fig. 2). The intensities of each hot spot and their calculated areas and temperatures are listed in Table 2. The detailed calculations and error estimates are available on the World Wide Web (*11*).

The uncertainties listed in Table 2 come from several sources. The eclipse images are generally noisy (Fig. 1) because of the intense radiation environment near Jupiter and the long exposure times and high gain states of the images. The most intense radiation "hits" are usually easily recognized because they form bright pixels or streaks without the smear pattern of the hot spots and stars, and these noise spikes are removed or avoided in the measurements. Nonthermal emissions also contribute to the SSI clear-filter images. We saw diffuse glows at the limb and over plumes, because of materials above the surface. Although these diffuse glows are often an order of magnitude fainter than the hot spots and are much more extended, it is possible, in principle, that gas concentrated over vents contributes substantially to the intensities. Nonthermal processes such as lightning in plumes might also occur. However, our thermal interpretation of these emissions is supported by several arguments. First, we saw the diffuse glows, but not the hot spots, in the eclipse images acquired through three short-wavelength color filters in orbit G7, suggesting that diffuse glows are not, at least in these cases, associated directly with bright areas we interpret to be hot spots. Second, there is evidence for temperatures >1500 K from observations at wavelengths longer than 1 μm, such as telescopic observations (*12*), and Galileo's Near Infrared Mapping Spectrometer (NIMS) (*13*, *14*). These temperatures are based on observations acquired over wavelengths from 0.7 to 5.0 μm, so they do not appear to be due to unusual emissions at a few discrete wavelengths. Third, the bright spots seen in eclipse occur near features known to be volcanically active from observations of plumes and surface changes (*5*, *6*). Fourth, there is a one-to-one correspondence between hot spots and low-albedo materials, which often have morphologies consistent with lava flows (*5*, *6*). Nevertheless, noise may be a substantial source of error to temperature estimates on faint spots. The error on the mean intensity for each spot is given in Table 2. Minimum and maximum temperatures were derived from 1σ errors with the error propagation on a ratio (*15*), except in the special case of Pillan in C9.

The most impressive and convincing high-temperature eruption was near Pillan Patera in orbit C9 (Fig. 1). The C9 eclipse observation experienced some complications, which turned out to be fortuitous for the temperature estimation. The image was an on-chip mosaic, in which the 1MC and clear exposures were acquired on the same frame. However, an error in the sequencing commands resulted in movement of the scan platform from the 1MC position to the clear position during the 1MC exposure. As a result, instead of a 25.6-s 1MC image on the left-hand side of the frame and a 6.4-s clear image on the right, we acquired a 13.8-s 1MC image on the left, 4 s of 1MC exposure while moving between positions, and 7.75 s of 1MC exposure at the clear position, followed by the 6.4-s clear exposure. A horizontal line connecting the Pillan hot spot images resulted from the 4-s 1MC exposure while moving. To estimate the clear intensities, we had to first subtract the 1MC intensity added to the clear-filter image. Pillan is the brightest hot spot on the disk and is saturated in both the 1MC and clear + 1MC images. Ordinarily

Table 1. SSI eclipse images used for temperature measurements. Dates are given as month/day/year. PICNO, picture number.

Orbit	Date	PICNO	Bandpass	Exposure time(s)	Scale (km/pixel)
G7	4/03/97	G7I0013	CLR	2.13	33.2
		G7I0011	1MC	6.4	33.2
G8	5/06/97	G8I0003	CLR	6.4	18.6
		G8I0001	1MC	6.4	18.6
C9	6/28/97	C9I0026	CLR	6.4*	14.6
		C9I0025	1MC	13.85	14.6
C10	9/19/97	C10I0045	CLR	6.4	11.4
		C10I0046	1MC	25.6	11.4
E11	11/08/97	E11I0027	CLR	6.4	13.8
		E11I0025	1MC	25.6	13.8
	11/08/97	E11I0028	CLR	0.27	13.8
		E11I0026	1MC	2.13	13.8

*Sequence error resulted in exposure through 1MC for 7.75 s on top of clear (CLR) image in C9.

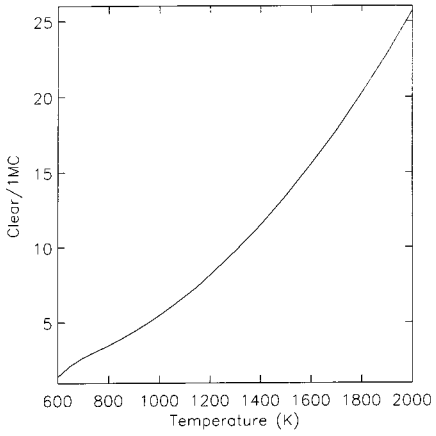

Fig. 2. Clear/1MC ratio of intensities versus blackbody temperature for the SSI ca mera.

Fig. 3. Three-temperature fit to NIMS spectrum of Pillan and Pele hot spots in orbit C9. Three blackbody curves are shown: dashed curve for 544-km^2 area at 475 K, dash-dot curve for 17.6-km^2 area at 975 K, and dash-dot-dot-dot curve for 0.11-km^2 area at 1825 K. The smooth solid curve is the sum of the three blackbody curves, and the asterisks mark the NIMS data points.

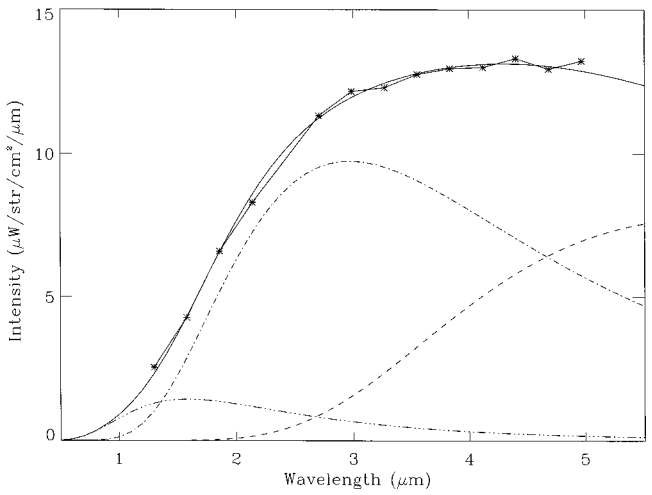

such saturation would preclude accurate measurement of the intensities. However, we were able to measure the 1MC intensity from the unsaturated horizontal line at 24.7 ± 3.66 electrons/s. In the clear image, the pixels are not just saturated, but two columns are "bleeding." Bleeding occurs when a pixel exceeds full well (100,000 to 120,000 electrons), so the excess electrons leak down the column (*9*). A minimum of 19 pixels bled, accounting for at least 1.9×10^6 electrons. Forty additional saturated (but not necessarily bleeding) pixels indicate 0.33×10^6 to 4.0×10^6 additional electrons, and unsaturated pixels add 0.4×10^6 electrons, for a total of between 2.6×10^6 and 6.3×10^6 electrons generated on the detector by the Pillan hot spot. Subtracting the 1MC contribution and dividing by exposure time yield a minimum intensity of 0.38×10^6 electrons/s, and a maximum intensity is 0.96×10^6 electrons/s through the clear filter. The minimum and maximum clear/1MC ratios (including adding and subtracting the potential 1MC error due to noise) are 13.4 and 45.4, corresponding to brightness temperatures of 1500 and 2600 K, respectively.

Additional evidence for these high temperatures comes from Galileo NIMS (*13*). Analysis of NIMS nighttime spectra of Io shows an especially high-temperature component, at least 1475 K, in several hot spots (*14*). The Pillan-Pele region was detected by NIMS in orbit C9 at low resolution (725 km/pixel), so the Pillan and Pele hot spots fall within a single NIMS pixel. Analysis of the nighttime spectrum with a two-component fit yields temperature and area models of 700 K (125 km^2) and 1450 K (1.1 km^2) but does not fit the spectrum well at the shorter wavelengths. The fit is improved by adding a third, hotter component (Fig. 3), yielding temperatures and areas of 475 K (544 km^2), 975 K (17.6 km^2), and 1825 K (0.11 km^2) for Pele and Pillan combined. Projected areas have been corrected for the viewing geometry, and errors for these fits are ±25 K and ±10% area. The 1825-K area (0.11 km^2 for Pillan and Pele) exceeds that derived from the SSI data, which gives 0.03 km^2 at 1825 K for Pillan alone. The NIMS and SSI observations were collected only 7 to 9 min apart, so the activity at Pillan changed over just a few minutes or Pele must also have a substantial area at these high temperatures.

IR brightness temperatures of 1500 to 1800 K imply liquid lava temperatures of at least 1700 to 2000 K because of the rapid cooling of lava surfaces (*16*), and our data do not preclude liquid temperatures hundreds of degrees higher. However, the hottest lavas that are common on Earth and the other terrestrial planets, basalts, are typically erupted at only 1300 to 1450 K (*17*). The hottest ancient terrestrial lavas, called komatiites (ultramafic lavas rich in magnesium), were erupted at 1700 to 1900 K (*18*), and the hottest lunar lavas (the orange and green glasses) were produced at about 1700 K (*19*).

Given our limited knowledge of the chemistry and structure of the interior of Io, any attempt to explain why such hot lavas are common on Io is necessarily speculative. However, the high lava temperatures

Table 2. Temperature-area models for SSI eclipse observations of Io. I_{CLR} and I_{1MC} are the intensities of each hot spot in the CLR and 1MC bandpass images. Uncertainties in these intensities and their ratio are listed in parentheses. Temperatures were estimated from the ratio through the curve in Fig. 2. Areas were computed by matching the CLR bandpass intensity to the predicted response of the SSI camera to a blackbody at the appropriate temperature and viewing geometry [see (*11*) for details]. *T*, temperature; T_{min}, minimum temperature; T_{max}, maximum temperature.

Hot spot name	Latitude, Longitude	Orbit	I_{CLR} (electrons/s)	I_{1MC} (electrons/s)	Ratio	Best *T*	Area (km^2)	T_{min}	T_{max}
Kanehekili-S	17°S, 36°	G7	6.27 (0.72)	1.3 (0.24)	4.82 (1.05)	940	9.8	830	1030
		G8	4.53 (0.13)	0.41 (0.11)	11.05 (2.98)	1375	0.009	1195	1530
Kanehekili-N	14°S, 33°	G7	>10.58 (0.72)	0.62 (0.24)	17.06 (6.71)	1660	>0.006	1335	1930
		G8	5.76 (0.13)	0.47 (0.11)	12.26 (2.88)	1440	0.006	1280	1580
Janus	4°S, 39°	G7	>3.98 (0.53)	0.53 (0.24)	7.51 (3.66)	1160	>0.21	840	1380
		G8	2.37 (0.13)	0.17 (0.11)	13.94 (9.05)	1525	0.0012	945	1900
Amirani	23°N, 116°	G8	2.94 (0.13)	0.17 (0.11)	17.29 (11.22)	1675	0.0006	1050	>2000
Svarog	54°S, 270°	C9	>27.81 (0.34)	4.04 (0.12)	6.88 (0.22)	1110	>0.87	1095	1130
Acala	11°N, 333°	C9	7.47 (0.30)	0.74 (0.14)	10.09 (1.95)	1320	0.019	1200	1430
Marduk	27°S, 209°	C9	0.89 (0.22)	0.27 (0.14)	3.30 (1.89)	780	25.4	600	975
	27°S, 209°	E11	4.42 (0.20)	0.33 (0.06)	13.39 (2.51)	1500	0.002	1365	1615
Pillan	10°S, 242°	C9	*	24.7 (3.66)	*	1825†	0.03	1500	>2600
		C10	71.6 (1.24)	15.1 (0.24)	4.74 (0.11)	930	16.3	920	945
Pillan-N	9°S, 243°	E11	2.88 (0.13)	0.23 (0.04)	12.52 (2.25)	1450	0.0012	1330	1560
Pillan-S	11°S, 242°	E11	15.9 (0.25)	1.63 (0.05)	9.75 (0.34)	1300	0.029	1280	1320
Pele	18°S, 256°	E11	261.1 (4.26)	27.9 (0.68)	9.36 (0.27)	1275	0.575	1260	1290
Lei-Kung	37°N, 203°	E11	1.59 (0.13)	0.13 (0.04)	12.23 (3.89)	1440	0.0016	1210	1625
Isum-N	33°N, 205°	E11	1.50 (0.12)	0.13 (0.04)	12.50 (4.31)	1450	0.0012	1205	1655
Isum-S	30°N, 207°	E11	1.12 (0.13)	0.11 (0.04)	10.18 (3.89)	1325	0.0025	1070	1530
–	22°N, 238°	E11	1.44 (0.13)	0.09 (0.04)	16.00 (7.26)	1620	0.0002	1240	1915

*The Pillan observation in orbit C9 is unusual (see text). †1825 K was chosen as best temperature for Pillan in C9 on the basis of fit to NIMS spectrum (Fig. 3).

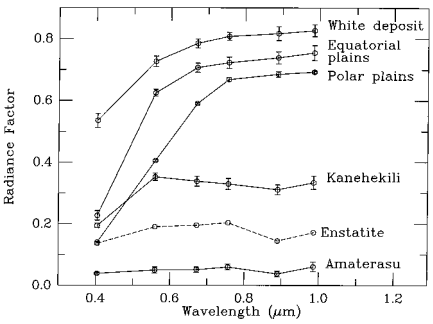

Fig. 4. Spectral reflectances on Io as seen with six SSI color filters. The bulk of Io's surface (white deposits and plains units) has a flat spectrum from 0.75 to 1.0 μm, but the dark features covering a few percent of the surface (such as Kanehekili and Amaterasu, shown here) are relatively dark in the 0.89-μm bandpass. The ultraviolet absorption at Kanehekili (drop in reflectance at 0.4 μm) is typical of all but the darkest features and is evidence for the presence of sulfurous materials in addition to silicates (*34*). Also shown is the spectrum for an enstatite (orthopyroxene) with 5% FeO (*35*) convolved to the SSI bandpasses and vertically scaled to place it between the Kanehekili and Amaterasu spectra.

may be a result of (i) the lava being heated far above its thermodynamic equilibrium temperature (that is, superheated) or (ii) the lava having a composition that has a high melting temperature.

On Earth, superheated lavas form when magma rises rapidly from depth and the adiabatic temperature gradient is less than the slope of the liquidus of the magma (*20*). For a dry basaltic liquid (with a melting temperature of ~1500 K at low pressure) to reach the surface of Io at 1700 to 2000 K, it must have been generated at a depth of 300 to 800 km (1.5 to 4 GPa) and then risen with no substantial heat loss. The intense tidal heating of Io also allows for the possibility of superheated lavas originating from shallower depths. If the tidal heating within a magma chamber is fast enough, the heat may go into raising the temperature of the liquid instead of melting the surrounding rocks. Tidal heating is likely to be concentrated near the lithosphere-asthenosphere boundary (*21*), a reasonable location for magma chambers to form by stalling at a density or rheological boundary (*22*). The difficulty in producing lavas superheated by hundreds of degrees is that such a large temperature contrast between the magma and its surroundings should result in rapid heat loss.

It is more likely that the lavas have a high melting temperature. Although a few isolated cases of high-temperature volcanism might be attributed to some rare, exotic composition such as metal sulfides, it is difficult to call on such an explanation for the large number of observed hot spots. Instead, given that Io's density is consistent with a silicate body broadly similar to other rocky bodies in our solar system (*23*), high-magnesium (ultramafic) silicates would be the most likely composition. Two models for Io's interior have different implications for the lava compositions.

One option is for the lavas to be produced by large degrees of partial melting (~40%) of a mantle that has undergone little differentiation after separation of an iron-rich core. This model is directly analogous to the formation of komatiites on Earth during the Archean and suggests that Io's interior is similar to that of early Earth (*24*). Io's mantle might have retained such a primitive composition if the vigorous volcanic activity continuously recycles the lithosphere back into the mantle (*25*).

The alternative is that the volcanic activity has strongly differentiated Io. Geochemical modeling of such differentiation predicts a ~50-km-thick, low-density crust rich in alkali elements, silica, and aluminum and a mantle rich in magnesium, iron, and calcium (*26*). The mantle could be further separated into a less dense, magnesium-rich upper part and a denser, iron- and calcium-rich section (*26*). Melts from this hypothetical upper mantle could have temperatures up to ~2100 K, several hundred degrees higher than those of komatiites.

The primitive and differentiated models of Io represent end-members, and the truth may lie somewhere in between. There are observations to support each model. The presence of an alkali- and silica-rich crust is supported by several observations: (i) the presence of sodium and potassium clouds around Io (*27*), (ii) a 1.25-μm absorption band consistent with feldspars (a family of alkali-rich alumino-silicate minerals) seen in the spectrum of Io away from hot spots (*28*), and (iii) the presence of a variety of landforms consistent with silica-rich volcanism (*29*). The large-scale topography of Io derived from Voyager data (*30*) has been interpreted as due to variations in the thickness of a low-density crust (*31*), but Galileo limb profiles have not confirmed the existence of this large-scale topography (*32*). The widely spaced mountains on Io could be due to low-density plutons (*26*) but suggest a relatively small volume of such differentiated material floating as isolated pods in a denser (and presumably more primitive) crust. If there is a differentiated crust, then the ultramafic volcanics should be concentrated in topographically low areas such as the calderas where the high-temperature hot spots are observed. It is difficult to explain how dense mantle melts could rise through a 50-km-thick low-density crust to reach the surface, but this has occurred on the Moon (*22*). Support for a more primitive crust comes from the presence and ubiquity of probable magnesium-rich lavas reported here, which is evidence for mixing between the crust and mantle. However, it is hard to estimate the fraction of lava that may be erupting at lower temperatures, more consistent with differentiated lavas, because the cooling of the higher temperature eruptions inevitably creates a suite of lower temperature surfaces as well.

Analysis of six-color spectra of Io from SSI supports the hypothesis that lavas erupting on Io contain magnesium-rich pyroxenes. Orthopyroxene (enstatite-hypersthene solid solution) has an absorption band near 0.9 μm in reflectance spectra (*33*), provided there is at least a small amount of iron present. SSI has spectral filters with effective wavelengths of 0.76, 0.89, and 0.99 μm, and the multispectral images reveal that, in the dark areas on Io, the reflectance is lower at 0.89 μm than at 0.76 or 0.99 μm (Fig. 4). Because the dark areas correspond to sites of active or recently active high-temperature volcanism and because magnesium-rich pyroxenes are common in ultramafic rocks, the SSI spectra are consistent with our interpretation that the high-temperature hot spots are caused by the eruption of ultramafic lavas.

References and Notes

1. D. B. Nash, M. H. Carr, J. Gradie, D. M. Hunten, C. F. Yoder, in *Satellites*, J. A. Burns and M. S. Matthews, Eds. (Univ. of Arizona Press, Tucson, AZ, 1990), pp. 629–688; A. S. McEwen *et al.*, in *Time-Variable Phenomena in the Jovian System*, M. J. S. Belton, R. A. West, J. Rahe, Eds. (NASA SP-494, NASA, Washington, DC, 1989), pp. 11–46.
2. J. C. Pearl and W. M. Sinton, in *Satellites of Jupiter*, D. Morrison, Ed. (Univ. of Arizona Press, Tucson, AZ, 1982), pp. 724–755.
3. T. V. Johnson *et al.*, *Science* **242**, 1280 (1988).
4. J. R. Spencer *et al.*, *Geophys. Res. Lett.* **24**, 2451 (1997); R. Lopes-Gautier *et al.*, *ibid.*, p. 2439.
5. A. S. McEwen *et al.*, *ibid.*, p. 2443.
6. A. S. McEwen *et al.*, *Icarus*, in press.
7. J. I. Lunine and D. J. Stevenson, *ibid.* **64**, 345 (1985).
8. M. H. Carr, *J. Geophys. Res.* **91**, 3521 (1986); D. L. Blaney, T. V. Johnson, D. L. Matson, G. J. Veeder, *Icarus* **113**, 220 (1995); A. G. Davies, *ibid.* **124**, 45 (1996); R. R. Howell, *ibid.* **127**, 394 (1997).
9. K. P. Klaasen *et al.*, *Opt. Eng.* **23**, 334 (1983); M. J. S. Belton *et al.*, *Space Sci. Rev.* **60**, 413 (1992); K. P. Klassen *et al.*, *Opt. Eng.* **36**, 3001 (1997).
10. M. J. S. Belton *et al.*, *Science* **274**, 377 (1996).
11. See www.sciencemag.org/feature/data/981109.shl for a complete table of values used to compute the intensity of each hot spot in each image.
12. G. J. Veeder, D. L. Matson, T. V. Johnson, D. L. Blaney, J. D. Goguen, *J. Geophys. Res.* **99**, 17095 (1994); J. A. Stansberry, J. R. Spencer, R. R. Howell, C. Dumas, D. Vakil, *Geophys. Res. Lett.* **24**, 2455 (1997).
13. R. W. Carlson *et al.*, *Space Sci. Rev.* **60**, 457 (1992); W. D. Smythe *et al.*, *J. Geophys. Res.* **100**, 18957 (1995).
14. A. G. Davies *et al.*, *Lunar Planet. Sci.* **XXIX** (1998) [available on CD-ROM].
15. P. R. Bevington, *Data Reduction and Error Analysis for the Physical Sciences* (McGraw-Hill, New York, 1969).
16. L. Keszthelyi and A. McEwen, *Geophys. Res. Lett.* **24**, 2463 (1997).
17. S. A. Morse, *Basalts and Phase Diagrams* (Springer-Verlag New York, 1980); see M. O. Garcia, T. P. Hulsebosch, and J. M. Rhodes [in *Mauna Loa Revealed, Geophys. Monogr. Ser.*, vol. 92, J. M. Rhodes and J. P. Lockwood, Eds. (American Geophysical Union, Washington, DC, 1995), pp. 219–240] for a description of olivine-rich submarine basalts with magma temperatures up to 1688 K.
18. P. C. Hess, *Origins of Igneous Rocks* (Harvard Univ. Press, Cambridge, MA, 1989); C. Herzberg, *J. Geophys. Res.* **97**, 4521 (1992).
19. G. Heiken, D. Vaniman, B. M. French, Eds., *Lunar Sourcebook: A Users' Guide to the Moon* (Cambridge Univ. Press, New York, 1991).
20. A. Hall, *Igneous Petrology* (Wiley, New York, 1987).
21. M. Segatz, T. Spohn, M. N. Ross, G. Schubert, *Icarus* **75**, 187 (1988).
22. J. W. Head and L. Wilson, *Geochim. Cosmochim. Acta* **56**, 2155 (1992).
23. B. A. Smith *et al.*, *Science* **204**, 951 (1979); J. D. Anderson, W. L. Sjogren, G. Schubert, *ibid.* **272**, 709 (1996).
24. D. L. Matson *et al.*, *Lunar Planet. Sci.* **XXIX** (1998) [available on CD-ROM].
25. M. H. Carr *et al.*, *Icarus*, in press.
26. L. Keszthelyi and A. McEwen, *ibid.* **130**, 437 (1997).
27. M. L. Johnson and D. S. Burnett, *Geophys. Res. Lett.* **17**, 981 (1990).
28. J. B. Pollack *et al.*, *Icarus* **36**, 271 (1978); R. W. Carlson *et al.*, *Geophys. Res. Lett.* **24**, 2479 (1997).
29. G. G. Schaber, in *Satellites of Jupiter*, D. Morrison, Ed. (Univ. of Arizona Press, Tucson, AZ, 1982), pp. 556–597.
30. R. W. Gaskell, S. P. Synnott, A. S. McEwen, G. G. Schaber, *Geophys. Res. Lett.* **15**, 581 (1988).
31. M. N. Ross, G. Schubert, T. Spohn, R. W. Gaskell, *Icarus* **85**, 309 (1990).
32. P. C. Thomas *et al.*, *ibid.*, in press.
33. J. B. Adams, *J. Geophys. Res.* **79**, 4829 (1974).
34. D. A. Rothery *et al.*, *ibid.* **101**, 26131 (1996).
35. Sample NMNH128288, U.S. Geological Survey, Denver Spectroscopy Laboratory; sample documented by T. V. V. King.

36. We thank G. J. Taylor and D. L. Blaney for helpful discussions. Supported by the Galileo project and by NASA's Planetary Geology and Geophysics program.

4 March 1998; accepted 14 May 1998